This is the accepted manuscript made available via CHORUS. The article has been published as:

Phase diagram of twisted bilayer math xmlns="http://www.w3.org/1998/Math/MathML">msub>mi>MoTe/mi>mn>2/mn>/msub>/math> in a magnetic field with an account for the electron-electron interaction

Minxuan Wang, Xiaoyu Wang, and Oskar Vafek

Phys. Rev. B **110**, L201107 — Published 15 November 2024

DOI: 10.1103/PhysRevB.110.L201107

Interacting phase diagram of twisted bilayer $MoTe_2$ in magnetic field

Minxuan Wang,[1,2] Xiaoyu Wang,[1] and Oskar Vafek[1,3]

[1] *National High Magnetic Field Lab, Tallahassee, FL 32310*
[2] *Department of Physics, University of California, Berkeley, CA 94720, USA*
[3] *Department of Physics, Florida State University, Tallahassee, FL 32306*

We study electron-electron interaction induced states of twisted bilayer $MoTe_2$ in an out-of-plane magnetic field $B\hat{\mathbf{z}}$ near one hole per moiré unit cell filling. The 3D phase diagram showing the evolution of competing phases with B, interaction strength and an out-of-plane electric field is presented at electron fillings that follow the Diophantine equation along Chern number $-\mathrm{sign}\,(B)$ line, that is pointing away from the charge neutral filling, where we find prominent Chern insulators consistent with the experiments. We also explain the experimental absence of prominent Chern insulators along the Chern number $+\mathrm{sign}\,(B)$ line.

Introduction.— Moiré materials are well known for their tunability and hosting various correlated phases due to their narrow energy electronic bands[1, 2]. Among these materials, twisted transition metal dichalcogenides (TMD) homobilayers, as well as heterobilayers, are predicted[3, 4], and experimentally shown, to exhibit integer quantum anomalous Hall (QAH) effect [5, 6]. Intriguingly, fractional quantum anomalous Hall effect has recently also been observed in twisted $MoTe_2$ homobilayer ($tMoTe_2$) [7–10], with a number of theoretical papers devoted to these integer and fractional Chern insulators[11–27]. Due to the large unit cell area A_{uc} of moiré materials, out-of-plane magnetic field $B\hat{\mathbf{z}}$ has proven to be a powerful probe of their correlated states [7, 8, 28, 29]. Particularly interesting is the evolution of such states in the ν-B plane, where the electron filling $\nu = \rho_e A_{uc}$ and ρ_e is the areal density of electrons. The key tool is the thermodynamic formula [30, 31] which states that the quantized Hall conductivity of a gapped state of electrons (with charge $-e$) at $T = 0$ follows

$$\sigma_{xy} = -\sigma_{yx} = -e\frac{\partial \rho_e}{\partial B}\bigg|_{\mu,T} = -t\frac{e^2}{h}. \tag{1}$$

Here t is the Chern number[32] and we use the SI units throughout. The Diophantine equation for ν is[33–37]

$$\nu = s + t\frac{\phi}{\phi_0}, \tag{2}$$

where the flux quantum $\phi_0 = h/e = 4136\mathrm{T}\cdot\mathrm{nm}^2$ and the flux through the unit cell is $\phi = BA_{uc}$.

A ubiquitous experimental observation in $tMoTe_2$ at twist angles in the $3.4^\circ \sim 3.9^\circ$ range is the QAH state at $\nu = -1 = s$ evolving into a Chern state at $B \neq 0$ with a prominent gap at $t = -\mathrm{sign}(B)$ and a noted absence of a prominent gap at $t = +\mathrm{sign}(B)$ [7–10]. In other words, the Streda lines emanating from $\nu = -1$ point *away* from the charge neutrality point (CNP) for either sign of B. The two QAH states with opposite Chern numbers at $B = 0$ are partners under the time reversal symmetry, which is spontaneously broken, and therefore they must be equally stable at $B = 0$. The relative instability of the $t = +\mathrm{sign}(B)$ state at $B \neq 0$ has thus far not been explained. Note that in 1.23° twisted WSe_2 bilayer the prominent Chern insulator line at $s = -1$ points *towards* the CNP[29], and that *both* behaviors have been observed in the magic angle twisted bilayer graphene device of Ref.[38], as well as in calculations [39].

Here we show that, within our $B \neq 0$ self-consistent Hartree-Fock calculation at the twist angle 3.89° and the dielectric constant ϵ entering the interaction (4) chosen to reproduce the $B = 0$ QAH state[23], the ground state at $s = -1$ and $t = -\mathrm{sign}(B)$ is valley polarized and that the holes preferentially populate the valley whose spin is aligned to the direction of the magnetic field. This state can be thought of as a Landau quantized QAH state with a non-vanishing (large) gap in the $B \to 0$ limit and we refer to it as a Chern paraelectric because it preserves $C_{2y}\mathcal{T}$, the combination of an in-plane 2-fold rotation symmetry and the time reversal symmetry. Its energy spectrum as a function of ϕ/ϕ_0 is shown in the Fig.2(a). Since the spin orientation of the holes in the two valleys is opposite due to the spin-valley locking[40], the valley polarization reverses upon reversing the sign of B (still at $t = -\mathrm{sign}(B)$). Interestingly, the nature of the lowest energy state at $s = -1$ and $t = +\mathrm{sign}(B)$ depends sensitively on g, the strength of the spin and orbital Zeeman coupling[41]. At $g = 0$, it is valley polarized but now the holes populate the valley whose spin is anti-aligned to the direction of the magnetic field. For a given B, it can be thought of as a Landau quantized time reversed partner of the QAH discussed above. Its (large) gap also does not vanish in the $B \to 0$ limit, see Fig.2(d). If it were stable, the valley polarization would reverse at a fixed B upon changing the filling from $-1 - \frac{|\phi|}{\phi_0}$ to $-1 + \frac{|\phi|}{\phi_0}$, similar to the observations reported in Ref.[42] in graphene heterostructures. Such a state would appear as a prominent Chern insulator, inconsistent with the experiments[7–10]. At $g \gtrsim 2$, however, the ground state changes and the holes populate the valley with spin aligned to the direction of the magnetic field for a range of B that expands to lower $|B|$ as g increases (Fig.2(h)). It can be thought of as an integer quantum Hall (IQH) state, populating the lowest pair of Landau levels (LLs) of the Chern paraelectric excitation spectrum at $t = -\mathrm{sign}(B)$ with electrons, as seen in the Fig.2(c).

Because of the sizable band mass, its gap is small and vanishing as $B \to 0$, consistent with the experimental absence of a prominent Chern insulator at $t = +\text{sign}(B)$ and presence at $t = -\text{sign}(B)$. As detailed below, we estimate the orbital Zeeman contribution to g in $tMoTe_2$ to be 3.23 and of the same sign as the spin contribution 2, placing us safely in the $g \gtrsim 2$ regime. We note that the sophisticated ab initio calculation[43] yields a total Lande g-factor $g = 9.17$, exceeding our estimate and placing the system deeper into the $g \gtrsim 2$ regime.

Perpendicular electric field, D, has also proved to be a powerful tool to probe and manipulate the nature of correlated states in $tMoTe_2$[7–10]. In the experiments at $B = 0$, the spin polarized QAH state transitions into a trivial insulator above a critical D_*[7–10]. The proximate trivial state is argued to be spin, and therefore valley, unpolarized in the Ref. [8] and spin, and therefore valley, polarized in the Ref. [10]. Such topological transition is also seen in the Hartree-Fock calculation at $B = 0$[23, 27], and the spin structure of the trivial state depends on the value of ϵ. For $\epsilon > \epsilon' \approx 19$ the transition is directly into a spin unpolarized intervalley coherent state (IVC) and for $\epsilon_* \approx 15.4 < \epsilon < \epsilon'$ the proximate trivial state is valley polarized (VP). This can be seen in the $B = 0$ plane of Fig.4 where we vary the D-induced potential difference between two layers u_D. Intriguingly, at $B \neq 0$ and $t = -\text{sign}(B)$ a sharp change of compressibility can be seen in the experiment at the same D_* as the transition at $B = 0$ (see Extended Data Fig.10 of Ref. [8]). Our calculation at $B \neq 0$ captures this effect. As shown in the Fig.3(a), at $\epsilon = 20$ chosen to recover the phenomenology of Ref.[8] at $B = 0$, we observe a crossover at D_* between a Chern paraelectric with a large gap and an ostensibly IQH state of a Landau quantized trivial insulator with one LL depopulated by electrons and a small gap. We refer to the latter as a QH ferroelectric because at $u_D = 0$ it breaks $C_{2y}\mathcal{T}$. Both states are spin polarized. The results of a separate Hartree-Fock calculation at $t = 0$ shown in the Fig.3(b) confirm the prominent trivial insulator with a large gap. Thus, the incompressible states can appear simultaneously at $\nu = -1$ and $\nu = -1 - \frac{|\phi|}{\phi_0}$ for a range of D near D_*.

In order to explore the robustness of the above results, as well as the tunability of the correlated phases, we perform the Hartree-Fock calculations at $s = -1$ and $t = -\text{sign}(B)$ at varying ϵ, u_D and B. The resulting tentative phase diagram is shown in the Fig.4. At $D = 0$ the first order topological transition at ϵ_* extends to $B \neq 0$ despite separating states with the same Chern number t at $B \neq 0$ because the QH ferroelectric on one side breaks $C_{2y}\mathcal{T}$ and the Chern paraelectric on the other does not. This first order phase transition moves towards stronger interaction as B increases, favoring the Chern paraelectric i.e. the descendant of the QAH state. The transition must also extend to small non-zero D despite the explicit breaking of $C_{2y}\mathcal{T}$ by D because it starts out first order at $D = 0$. Indeed, Fig.3(c) shows the jump in the layer polarization at a fixed B persisting to non-zero

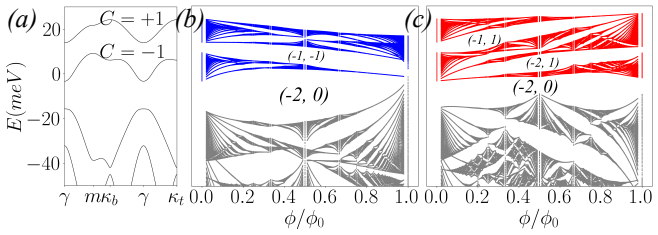


FIG. 1. (a) Band structure at $B = 0$ in the valley $\mathbf{K}$ for $tMoTe_2$ at $\theta = 3.89°$.(b,c) Hofstader spectra at $\mathbf{K}$ and $\mathbf{K}'$, omitting Zeeman effect.

u_D, with D favoring the ferroelectric and the first order transition terminating at a critical endpoint. As we show below, we can describe this using a simple Landau theory for an Ising ferroelectric with a negative quartic coupling. Upon varying B the critical endpoint extends to the red curve shown in the Fig.4. Interestingly, the D induced crossover shown in the Fig.3(a) appears at B and ϵ notably separated from the critical endpoint. We understand it as crossing the Widom line, defined as the peak in the layer polarizability, extending beyond the critical endpoint as shown in the Figs.3(d) and 4. As IVC is strongly suppressed by the B-field, Chern paraelectric and QH ferroelectric are the main phases in the Fig.4. Below we discuss our formalism and computational scheme that lead to the above results. We note in passing that at the twist angle 3.89°, $\phi = \phi_0$ at $B \simeq 176$T, so to get below 9T as in the experiments we need $\phi/\phi_0 \lesssim 1/20$. Reaching such a small flux efficiently in our interacting calculation is enabled by a recently developed technique[44–46] utilizing the $B = 0$ hybrid Wannier states to construct the basis at $B \neq 0$; some of our calculations go down to $\phi/\phi_0 = 1/47$.

Continuum model— The moiré bands of experimental relevance originate from the spin-valley locked valence bands of monolayer $MoTe_2$[47]. The relations in Eq. (1) and Eq. (2), as well as the stated experimental results, hold in any right handed coordinate system (even though σ_{xy}, and therefore t, changes sign between two coordinate system choices related by a 180° rotation about x or y axis). We are therefore free to choose any of the two out-of-plane directions as $\hat{\mathbf{z}}$ and we made the common choice [47] of aligning it with the spin angular momentum direction of the valley $\mathbf{K}$. Then, in valley $\mathbf{K}$ and for spin up, the non-interacting moiré band structure can be described by a continuum electronic model [3]:

$$H_{\mathbf{K}} = \int \mathrm{d}^2\mathbf{r} \begin{pmatrix} \psi^\dagger_{b\mathbf{K}}(\mathbf{r}) & \psi^\dagger_{t\mathbf{K}}(\mathbf{r}) \end{pmatrix} \times \begin{pmatrix} h_b(\mathbf{p}) + \Delta_b(\mathbf{r}) + \frac{u_D}{2} & \Delta_T(\mathbf{r}) \\ \Delta^*_T(\mathbf{r}) & h_t(\mathbf{p}) + \Delta_t(\mathbf{r}) - \frac{u_D}{2} \end{pmatrix} \begin{pmatrix} \psi_{b\mathbf{K}}(\mathbf{r}) \\ \psi_{t\mathbf{K}}(\mathbf{r}) \end{pmatrix}. \tag{3}$$

Here $\psi^\dagger_{l\mathbf{K}}(\mathbf{r})$ creates an electron in layer $l = b, t$, in valley $\mathbf{K}$, and at position $\mathbf{r}$. $h_l(\mathbf{p}) = -(\mathbf{p} - \hbar\kappa_l)^2/2m^*$ is kinetic energy, with $\mathbf{p} = -i\hbar\nabla_{\mathbf{r}}$ and effective

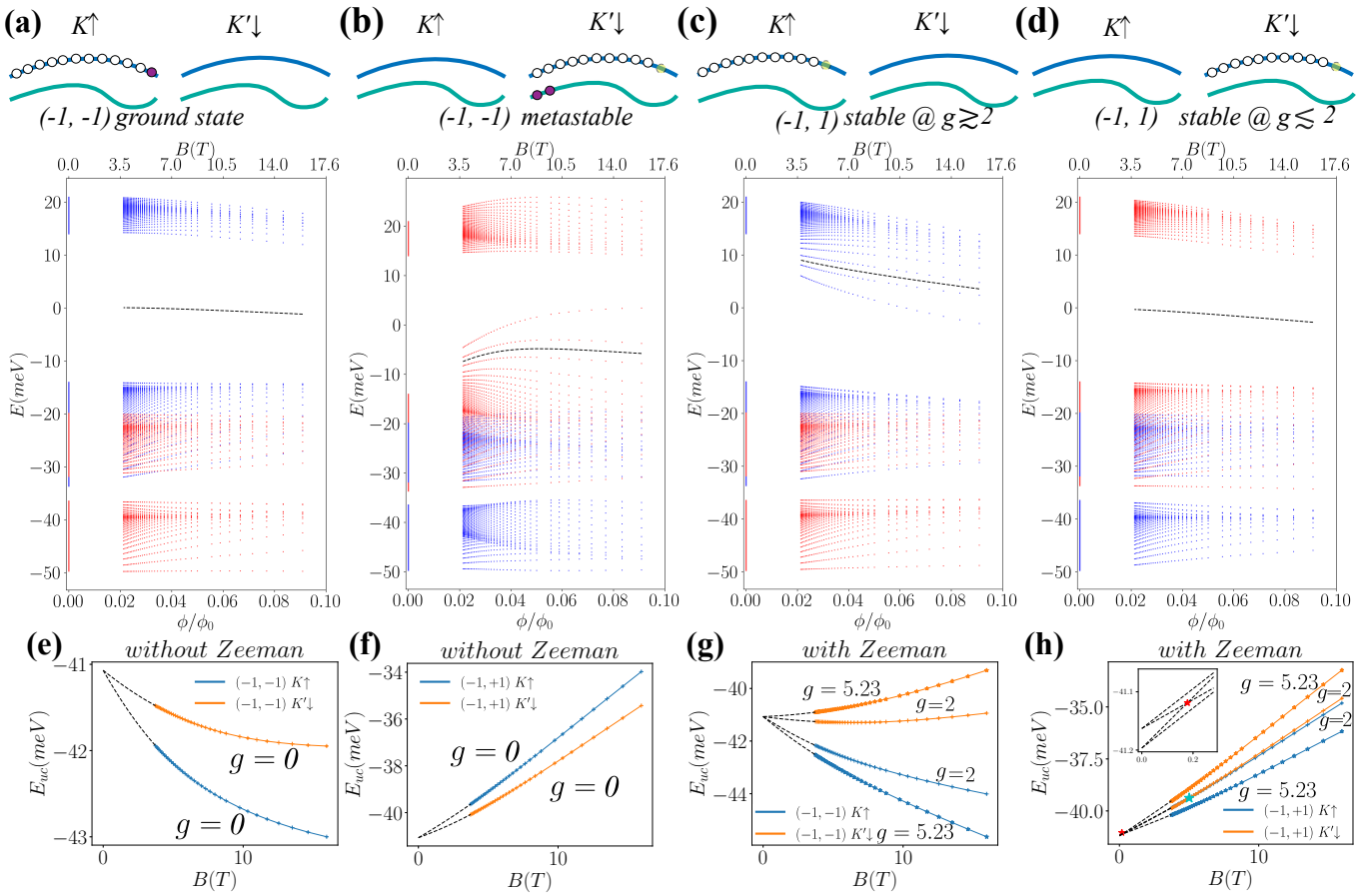


FIG. 2. (a-d)Hartree Fock energy spectrum with varying magnetic field at $\nu = -1 - \frac{|\phi|}{\phi_0}$ and $\nu = -1 + \frac{|\phi|}{\phi_0}$. Electrons occupy all eigenstates below black dashed line (guide to eye). Blue (red) points represent eigenstates in $\mathbf{K}(\mathbf{K}')$ valley. (e,f)Total energy per unit cell versus magnetic field. Dashed lines are obtained from quadratic interpolation using calculated energy per unit cell at $B = 0$. (g,h)Energy per unit cell with non-zero g factor.

mass m^*. κ_l points sit at the corners of the hexagonal moiré Brillouin zone, we describe the effect of D by adding a potential difference u_D between two layers, $\Delta_{b(t)}(\mathbf{r}) = 2V\sum_{j=1,3,5}\cos(\mathbf{G}_j\cdot\mathbf{r}\pm\phi)$ is the intralayer potential for bottom(top) layer, and $\Delta_T(\mathbf{r}) = w(1+e^{-i\mathbf{G}_2\cdot\mathbf{r}}+e^{-i\mathbf{G}_3\cdot\mathbf{r}})$ is interlayer tunneling potential. The reciprocal lattice vector $\mathbf{G}_j$ is obtained by counterclock-wise rotation of $\mathbf{G}_1 = 4\pi/(\sqrt{3}a_M)\hat{\mathbf{x}}$ by angle $(j-1)\pi/3$. $a_M = a_0/\theta$[rad] is moiré superlattice constant, where a_0 is the lattice constant of monolayer $MoTe_2$. We choose parameters $(a_0, m^*, V, \phi, \omega) = (0.355\text{nm}, 0.62m_e, 17.0\text{meV}, +107.7°, -16.0\text{meV})$ at twist angle $\theta = 3.89°$ [23]. The non-interacting model in the $\mathbf{K}'$ valley and for spin down is related by time reversal symmetry $\mathcal{T}$, which takes the complex conjugation of the 2×2 Hamiltonian in Eq. (3).

In an external magnetic field, we replace $\mathbf{p} \to \mathbf{p} + e\mathbf{A}$, where $\nabla\times\mathbf{A} = B\hat{\mathbf{z}}$, and add Zeeman coupling $\frac{1}{2}g\mu_B B\tau_0\sigma_z$, where τ_0 is the identity Pauli matrix acting on layer degrees of freedom, and σ_z is the spin Pauli matrix. At $B = 0$, the Hamiltonian is invariant under three-fold out-of-plane rotation C_{3z}, in-plane 2-fold rotation symmetry about the y-axis C_{2y} and the time reversal symmetry $\mathcal{T}$. At this order the continuum Hamiltonian also has a pseudo-inversion symmetry[19, 48] $\mathcal{I}$ given by $\mathbf{r}\to-\mathbf{r}$ in each valley and flipping the layers with τ_1. While both C_{2y} and $\mathcal{T}$ are broken at $B\neq 0$, their product $C_{2y}\mathcal{T}$ is preserved, as are C_{3z} and $\mathcal{I}$.

Fig. 1(a) shows the non-interacting band structure at $B = 0$ in the valley $\mathbf{K}$ where the two uppermost bands carry Chern number $+1$ and -1. The band dispersion and Chern numbers in the opposite valley $\mathbf{K}'$ are related by $\mathcal{T}$. For $B > 0$ the corresponding Hofstadter spectra for the valleys $\mathbf{K}$ and $\mathbf{K}'$, together with the (s,t) labels of the gaps, are shown in Fig. 1(b) and (c) respectively. As can be seen by the evolution of the magnetic subbands, a Chern band gains or loses states per unit cell according to the relation $1 + t\phi/\phi_0$. To study correlated phenomena, we project the Coulomb interaction onto the upper two Chern ±1 bands of both valleys if at $B = 0$, i.e. two bands per valley, or the magnetic subbands emanating

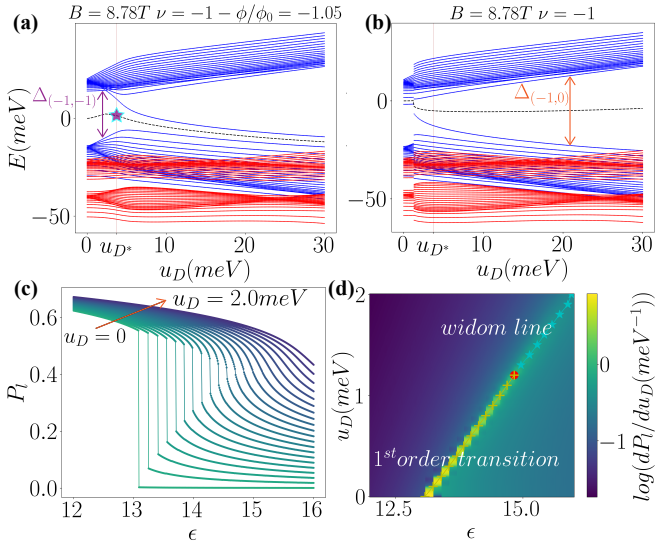


FIG. 3. (a)Hartree Fock spectrum at $\epsilon = 20$ with varying u_D at $\nu = -1 - \frac{|\phi|}{\phi_0}$ and (b) $\nu = -1$. Topological phase transition at $B = 0$ is at u_{D^*}. (c,d) Layer polarization P_l and polarizability with varying u_D and ϵ at $B = 8.78$T.

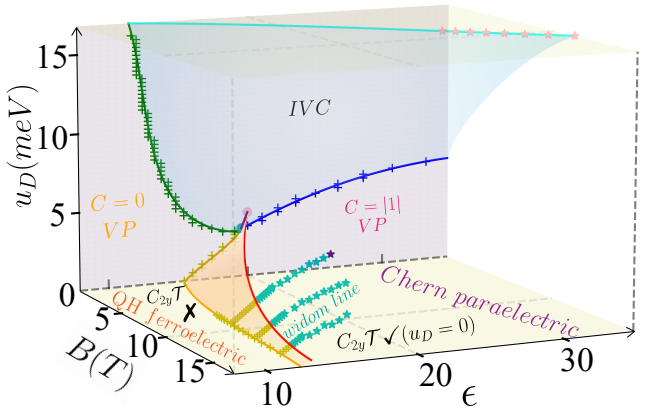


FIG. 4. Tentative phase diagram of $tMoTe_2$ at $\nu = -1 - \frac{|\phi|}{\phi_0}$ and 3.89° twist. The blue surface at $B \neq 0$ denotes the boundary between IVC state and two valley $U(1)$ preserving states, Chern paraelectric and QH ferroelectric.

from these Chern bands if at $B \neq 0$,

$$H_V = \frac{e^2}{4\epsilon\epsilon_0 A}\sum_{\mathbf{q}\neq 0}\frac{1}{|\mathbf{q}|}\tanh\left(|\mathbf{q}|d\right) : \mathcal{P}\rho_{\mathbf{q}}\rho_{-\mathbf{q}}\mathcal{P} : . \qquad (4)$$

Here $\rho_{\mathbf{q}} = \sum_{\eta,l}\int \mathrm{d}^2\mathbf{r} e^{-i\mathbf{q}\cdot\mathbf{r}}\psi^\dagger_{l\eta}(\mathbf{r})\psi_{l\eta}(\mathbf{r})$ is the Fourier transform of the electron density operator, with $\eta = \mathbf{K}$ or $\mathbf{K}'$, and total area A. In this work we consider a dual gate screened Coulomb interaction, d being the distance between each gate and $tMoTe_2$, taken to be 30nm in our calculations, with the small distance between the two $MoTe_2$ layers neglected. Symbol :: denotes operator normal ordering with respect to the charge neutrality[19]. $\mathcal{P}$ projects onto the mentioned Hilbert subspace which can be generated at $B \neq 0$ by solving the non-interacting problem[29, 44, 45]. At the B values of interest here, expanding $\mathcal{P}$ in the LL basis proves to be computationally expensive when dealing with interactions. Instead, we construct the basis states using the $B = 0$ hybrid Wannier states method following Ref. [45, 46].

Streda line near $\nu = -1$ and Zeeman effect— The $B > 0$ energy spectrum of candidate Chern states along the $(-1, \mp 1)$ lines is shown in Fig. 2(a-d). We present their total energy per unit cell as a function of B at varying Zeeman g factors in Fig. 2(e-h). The orbital contribution to the Zeeman effect stems from d-orbital nature of the states in each valley[47]. The two-band $\mathbf{k}\cdot\mathbf{p}$ Hamiltonian describing the large semiconductor gap in $MoTe_2$ monolayer has the form of a massive 2+1D Dirac Hamiltonian[47], whose minimal coupling to a low B-field results in an additional $\frac{1}{2}\hbar\omega_c$ energy shift compared to a Schrodinger Hamiltonian. Since the Dirac mass effectively flips sign between different valleys, this orbital shift also flips sign; it adds to the usual spin Zeeman factor of 2 (see Ref. [46] for details). Using the known effective mass of $MoTe_2$ we find it to be 3.23 and thus the total $g = 5.23$. Using the computed ground state energy of the QAH state at $B = 0$, we smoothly interpolate between the calculated energies at $B \neq 0$ and $B = 0$ at $g = 0$ using at most a second order polynomial in B as shown by the dashed lines in Fig.2(e,f). Because the Chern paraelectrics are fully valley polarized, their Zeeman energy can be obtained analytically. We can therefore find the critical B below which the valley switches for Chern paralectrics. As seen in the Fig.2(g,h) the crossing only occurs for the $(-1, 1)$ line. While at $g = 2$ it occurs at 5.01T (cyan star), at the more realistic $g = 5.23$ it is $\sim$ 178mT (red star). Thus any putative density induced valley switching would occur in the regime where the effects of quenched disorder dominate in realistic devices[9, 10], likely modifying the clean limit energetics obtained here.

Effects due to D-field— Energy spectrum induced by the perpendicular electric field D at $\phi/\phi_0 = 1/20$, corresponding to $B = 8.78T$, is shown in Fig. 3(a) along the $(-1, -1)$ line. The lowest unoccupied LL can be seen to detach from the unoccupied LL group as D increases and to closely approach the highest occupied LL. This is similar to the magnetic subband spectrum of an electron confined to move in a plane in a periodic potential and an out-of-plane uniform magnetic flux slightly smaller than ϕ_0 shown in the Fig. 7 of Ref.[49] as the strength of the periodic potential increases and drives a transition from a Chern insulator (a broadened LL) and a trivial insulator at their $\phi = \phi_0$. As shown in the Fig. 3(b) for $(-1, 0)$, a prominent trivial insulator is indeed stabilized in our Hartree-Fock calculation as well.

The evolution of the layer polarization $P_l = \frac{A_{uc}}{A}\sum_\eta \int \mathrm{d}^2\mathbf{r}\langle\psi^\dagger_{b\eta}(\mathbf{r})\psi_{b\eta}(\mathbf{r}) - \psi^\dagger_{t\eta}(\mathbf{r})\psi_{t\eta}(\mathbf{r})\rangle$ and polarizability dP_l/du_D at $(-1, -1)$ with varying ϵ and D, at a fixed $B = 8.78T$, are shown in Fig. 3(c,d). The main

features can be captured by a simple Landau theory for an Ising order parameter, odd under $C_{2y}\mathcal{T}$,

$$\delta E = -\gamma u_D P_l + \frac{a(\epsilon)}{2} P_l^2 - \frac{b}{4} P_l^4 + \frac{1}{6} P_l^6. \qquad (5)$$

Here γ and b are positive constants, and the prefactor of P_l^6 was used to rescale the energy units. Decreasing a with decreasing ϵ causes the spontaneous symmetry breaking at $u_D \propto D = 0$ via a 1^{st} order phase transition due to the negative quartic term. At the critical endpoint, the local minima merge (see Ref.[46]).

Phase diagram— The tentative 3D phase diagram along the $(-1,-1)$ line is shown in the Fig. 4. Markers correspond to parameters at which the transition, or a crossover in the case of Widom line, was calculated within Hartree Fock. The solid lines and surfaces are interpolated based on physical arguments. At $u_D \propto D = 0$ the Chern paraelectric and the quantum Hall ferroelectric are distinguished by P_l, a Landau order parameter, and so must be separated by a phase transition. At $u_D \neq 0$ however, it is possible to transform one to another without encountering a phase transition by avoiding the (orange) surface of 1^{st} order phase transitions terminating in the (red) critical endpoint curve. The IVC is a sharply defined phase at any B and D because it breaks valley $U(1)$ symmetry, preserved by B and D while the other phase(s) do not break it. It is suppressed by B even at $g = 0$, and further suppressed by the Zeeman effect. Therefore, while all the lines are computed at $g = 5.23$, the (cyan) phase boundary at $u_D = 16.8$meV is extrapolated from the $g = 2$ markers; it moves closer to the $B = 0$ plane at higher g (see Ref.[46]).

Discussion— Our calculation explains the presence of the $(-1,-1)$ line and the absence of the $(-1,+1)$ line in the experiments[7–10]. It also demonstrates the delicate balance between the energies of competing Chern states at $(-1,+1)$ polarized to opposite valleys, with the orbital Zeeman contribution ultimately deciding on the ground state with the small gap. Recent calculations[48, 50, 51] pointed out a rich evolution of the Chern bands and a lattice relaxation playing increasingly important role at low twist angles. While the Zeeman contribution is expected to be the same in the low angle regime, the energetic differences due to the magnetic subbands shown in our Fig.2(e,f) will change. It would be interesting to explore the possibility of density induced switching of the Chern number at different angles or different homobilayers using the framework developed here.

Acknowledgement— We thank B. Andrei Bernevig, Fengcheng Wu, Di Xiao, Jian Kang, Eslam Khalaf, Jiabin Yu, Daniel Parker, Kin Fai Mak, Jie Shan, and Xiaodong Xu for helpful discussions. M.W. sincerely thanks Taige Wang for fruitful discussions and ongoing collaborations. X.W. acknowledges financial support from the National High Magnetic Field Laboratory through NSF Grant No. DMR-2128556 and the State of Florida. O.V. was funded by the Gordon and Betty Moore Foundation's EPiQS Initiative Grant GBMF11070. Part of the numerical computations were carried out on resources provided by the Planck clusters at Florida State University. M.W. acknowledge the Beijing Paratera Co., Ltd. for providing HPC resources that have contributed to the research results reported within this paper.

[1] L. Balents, C. R. Dean, D. K. Efetov, and A. F. Young, Superconductivity and strong correlations in moiré flat bands, Nature Physics **16**, 725 (2020).
[2] D. M. Kennes, M. Claassen, L. Xian, A. Georges, A. J. Millis, J. Hone, C. R. Dean, D. Basov, A. N. Pasupathy, and A. Rubio, Moiré heterostructures as a condensed-matter quantum simulator, Nature Physics **17**, 155 (2021).
[3] F. Wu, T. Lovorn, E. Tutuc, I. Martin, and A. MacDonald, Topological insulators in twisted transition metal dichalcogenide homobilayers, Physical review letters **122**, 086402 (2019).
[4] T. Devakul, V. Crépel, Y. Zhang, and L. Fu, Magic in twisted transition metal dichalcogenide bilayers, Nature communications **12**, 6730 (2021).
[5] T. Li, S. Jiang, B. Shen, Y. Zhang, L. Li, Z. Tao, T. Devakul, K. Watanabe, T. Taniguchi, L. Fu, *et al.*, Quantum anomalous hall effect from intertwined moiré bands, Nature **600**, 641 (2021).
[6] Y.-M. Xie, C.-P. Zhang, J.-X. Hu, K. F. Mak, and K. T. Law, Valley-polarized quantum anomalous hall state in moiré mote 2/wse 2 heterobilayers, Physical Review Letters **128**, 026402 (2022).
[7] J. Cai, E. Anderson, C. Wang, X. Zhang, X. Liu, W. Holtzmann, Y. Zhang, F. Fan, T. Taniguchi, K. Watanabe, *et al.*, Signatures of fractional quantum anomalous hall states in twisted mote2, Nature **622**, 63 (2023).
[8] Y. Zeng, Z. Xia, K. Kang, J. Zhu, P. Knüppel, C. Vaswani, K. Watanabe, T. Taniguchi, K. F. Mak, and J. Shan, Thermodynamic evidence of fractional chern insulator in moiré mote2, Nature **622**, 69 (2023).
[9] H. Park, J. Cai, E. Anderson, Y. Zhang, J. Zhu, X. Liu, C. Wang, W. Holtzmann, C. Hu, Z. Liu, *et al.*, Observation of fractionally quantized anomalous hall effect, Nature **622**, 74 (2023).
[10] F. Xu, Z. Sun, T. Jia, C. Liu, C. Xu, C. Li, Y. Gu, K. Watanabe, T. Taniguchi, B. Tong, *et al.*, Observation of integer and fractional quantum anomalous hall effects in twisted bilayer mote 2, Physical Review X **13**, 031037 (2023).
[11] T. Neupert, L. Santos, C. Chamon, and C. Mudry, Fractional quantum hall states at zero magnetic field, Phys. Rev. Lett. **106**, 236804 (2011).
[12] D. Sheng, Z.-C. Gu, K. Sun, and L. Sheng, Fractional quantum hall effect in the absence of landau levels, Nature communications **2**, 389 (2011).
[13] N. Regnault and B. A. Bernevig, Fractional chern insu-

lator, Phys. Rev. X **1**, 021014 (2011).
[14] E. Tang, J.-W. Mei, and X.-G. Wen, High-temperature fractional quantum hall states, Phys. Rev. Lett. **106**, 236802 (2011).
[15] K. Sun, Z. Gu, H. Katsura, and S. Das Sarma, Nearly flatbands with nontrivial topology, Phys. Rev. Lett. **106**, 236803 (2011).
[16] A. Abouelkomsan, E. J. Bergholtz, and S. Chatterjee, Multiferroicity and topology in twisted transition metal dichalcogenides, Phys. Rev. Lett. **133**, 026801 (2024).
[17] C. Wang, X.-W. Zhang, X. Liu, Y. He, X. Xu, Y. Ran, T. Cao, and D. Xiao, Fractional chern insulator in twisted bilayer mote _2, arXiv preprint arXiv:2304.11864 (2023).
[18] V. Crépel and L. Fu, Anomalous hall metal and fractional chern insulator in twisted transition metal dichalcogenides, Physical Review B **107**, L201109 (2023).
[19] J. Yu, J. Herzog-Arbeitman, M. Wang, O. Vafek, B. A. Bernevig, and N. Regnault, Fractional chern insulators versus nonmagnetic states in twisted bilayer mote 2, Physical Review B **109**, 045147 (2024).
[20] H. Goldman, A. P. Reddy, N. Paul, and L. Fu, Zero-field composite fermi liquid in twisted semiconductor bilayers, Physical Review Letters **131**, 136501 (2023).
[21] W.-X. Qiu, B. Li, X.-J. Luo, and F. Wu, Interaction-driven topological phase diagram of twisted bilayer mote 2, Physical Review X **13**, 041026 (2023).
[22] T. Wang, T. Devakul, M. P. Zaletel, and L. Fu, Topological magnets and magnons in twisted bilayer mote _2 and wse _2, arXiv preprint arXiv:2306.02501 (2023).
[23] T. Wang, M. Wang, W. Kim, S. G. Louie, L. Fu, and M. P. Zaletel, Topology, magnetism and charge order in twisted mote2 at higher integer hole fillings (2023), arXiv:2312.12531 [cond-mat.str-el].
[24] F.-R. Fan, C. Xiao, and W. Yao, Orbital chern insulator at ν=- 2 in twisted mote 2, Physical Review B **109**, L041403 (2024).
[25] X. Liu, C. Wang, X.-W. Zhang, T. Cao, and D. Xiao, Gate-tunable antiferromagnetic chern insulator in twisted bilayer transition metal dichalcogenides, arXiv preprint arXiv:2308.07488 (2023).
[26] X.-J. Luo, W.-X. Qiu, and F. Wu, Majorana zero modes in twisted transition metal dichalcogenide homobilayers, Physical Review B **109**, L041103 (2024).
[27] B. Li, W.-X. Qiu, and F. Wu, Electrically tuned topology and magnetism in twisted bilayer mote 2 at ν h= 1, Physical Review B **109**, L041106 (2024).
[28] X. Lu, B. Lian, G. Chaudhary, B. A. Piot, G. Romagnoli, K. Watanabe, T. Taniguchi, M. Poggio, A. H. MacDonald, B. A. Bernevig, *et al.*, Multiple flat bands and topological hofstadter butterfly in twisted bilayer graphene close to the second magic angle, Proceedings of the National Academy of Sciences **118**, e2100006118 (2021).
[29] B. A. Foutty, C. R. Kometter, T. Devakul, A. P. Reddy, K. Watanabe, T. Taniguchi, L. Fu, and B. E. Feldman, Mapping twist-tuned multi-band topology in bilayer wse _2, arXiv preprint arXiv:2304.09808 (2023).
[30] P. Streda, Theory of quantised hall conductivity in two dimensions, Journal of Physics C: Solid State Physics **15**, L717 (1982).
[31] A. Widom, Thermodynamic derivation of the hall effect current, Physics Letters A **90**, 474 (1982).
[32] M. Kohmoto, Topological invariant and the quantization of the hall conductance, Annals of Physics **160**, 343 (1985).
[33] G. H. Wannier, A result not dependent on rationality for bloch electrons in a magnetic field, physica status solidi (b) **88**, 757 (1978).
[34] D. J. Thouless, Quantization of particle transport, Phys. Rev. B **27**, 6083 (1983).
[35] A. H. MacDonald, Landau-level subband structure of electrons on a square lattice, Phys. Rev. B **28**, 6713 (1983).
[36] Z. Tešanović, F. Axel, and B. I. Halperin, "hall" crystal versus wigner crystal, Phys. Rev. B **39**, 8525 (1989).
[37] E. M. Spanton, A. A. Zibrov, H. Zhou, T. Taniguchi, K. Watanabe, M. P. Zaletel, and A. F. Young, Observation of fractional chern insulators in a van der waals heterostructure, Science **360**, 62 (2018).
[38] Y. Xie, A. T. Pierce, J. M. Park, D. E. Parker, E. Khalaf, P. Ledwith, Y. Cao, S. H. Lee, S. Chen, P. R. Forrester, K. Watanabe, T. Taniguchi, A. Vishwanath, P. Jarillo-Herrero, and A. Yacoby, Fractional chern insulators in magic-angle twisted bilayer graphene, Nature **600**, 439–443 (2021).
[39] X. Wang and O. Vafek, Theory of correlated chern insulators in twisted bilayer graphene (2023), arXiv:2310.15982 [cond-mat.mes-hall].
[40] D. Xiao, G.-B. Liu, W. Feng, X. Xu, and W. Yao, Coupled spin and valley physics in monolayers of mos_2 and other group-vi dichalcogenides, Phys. Rev. Lett. **108**, 196802 (2012).
[41] H. Pan, F. Wu, and S. D. Sarma, Band topology, hubbard model, heisenberg model, and dzyaloshinskii-moriya interaction in twisted bilayer wse 2, Physical Review Research **2**, 033087 (2020).
[42] H. Polshyn, J. Zhu, M. A. Kumar, Y. Zhang, F. Yang, C. L. Tschirhart, M. Serlin, K. Watanabe, T. Taniguchi, A. H. MacDonald, and A. F. Young, Electrical switching of magnetic order in an orbital chern insulator, Nature **588**, 66–70 (2020).
[43] S. Zhang, H. Sheng, Z.-D. Song, C. Liang, Y. Jiang, S. Sun, Q. Wu, H. Weng, Z. Fang, X. Dai, *et al.*, Vasp2kp: k p models and landé g-factors from ab initio calculations, Chinese Physics Letters **40**, 127101 (2023).
[44] X. Wang and O. Vafek, Narrow bands in magnetic field and strong-coupling hofstadter spectra, Physical Review B **106**, L121111 (2022).
[45] X. Wang and O. Vafek, Revisiting bloch electrons in magnetic field: Hofstadter physics via hybrid wannier states, arXiv preprint arXiv:2303.16347 (2023).
[46] See supplemental material for orbital contribution to g factor, landau theory of transition between chern paraelectric and ferroelectirc, as well as hybrid wannier basis at finite magnetic field.
[47] D. Xiao, G.-B. Liu, W. Feng, X. Xu, and W. Yao, Coupled spin and valley physics in monolayers of mos 2 and other group-vi dichalcogenides, Physical review letters **108**, 196802 (2012).
[48] Y. Jia, J. Yu, J. Liu, J. Herzog-Arbeitman, Z. Qi, N. Regnault, H. Weng, B. A. Bernevig, and Q. Wu, Moir\'e fractional chern insulators i: First-principles calculations and continuum models of twisted bilayer mote _2, arXiv preprint arXiv:2311.04958 (2023).
[49] Z. Tešanović, F. Axel, and B. Halperin, "hall crystal"versus wigner crystal, Physical Review B **39**, 8525 (1989).
[50] X.-W. Zhang, C. Wang, X. Liu, Y. Fan, T. Cao, and D. Xiao, Polarization-driven band topology evo-

lution in twisted mote _2 and wse _2, arXiv preprint arXiv:2311.12776 (2023).
[51] N. Mao, C. Xu, J. Li, T. Bao, P. Liu, Y. Xu, C. Felser, L. Fu, and Y. Zhang, Lattice relaxation, electronic structure and continuum model for twisted bilayer mote _2, arXiv preprint arXiv:2311.07533 (2023).